Royal Netherlands
Meteorological Institute
*Ministry of Infrastructure
and Water Management*

Ozone Monitoring Instrument Algorithm Theoretical Basis Document of the Aerosol Direct Radiative Effect over clouds

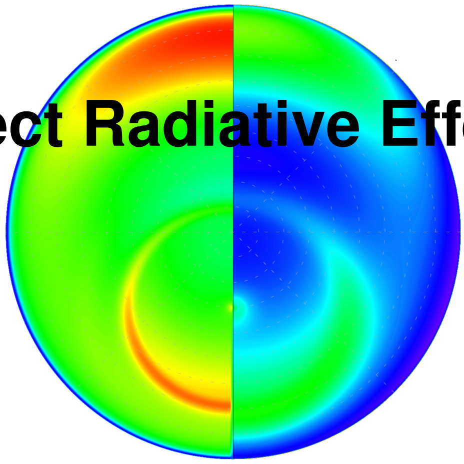

document number	:	OMI-KNMI-L2-0000-DRE
authors	:	M. de Graaf
CI identification	:	*None*
issue	:	0.0.1
date	:	2020-07-28
status	:	in preparation

Document approval record

	digital signature
Prepared:	
Checked:	
Approved PM:	
Approved PI:	

Document change record

issue	date	item	comments
0.0.1	2020-04-14	All	Initial version

Contents

List of Tables

List of Figures

1 Introduction

1.1 Identification

This document is identified as OMI-KNMI-L2-0000-DRE.

1.2 Purpose and objective

The purpose of this document is to describe the theoretical basis and the implementation of the OMI Level-2 Aerosol Direct Radiative Effect algorithm for OMI, combined with collocated MODIS measurements.

1.3 Document overview

[*generic description of the document*]

2 Applicable and reference documents

2.1 Reference documents

[RD1] M. de Graaf, L. G. Tilstra, I. Aben *et al.*; Satellite observations of the seasonal cycles of absorbing aerosols in Africa related to the monsoon rainfall, 1995 - 2008. *Atmos. Environ.*; **44** (2010) (10), 1274; doi:10.1016/j.atmosenv.2009.12.03.

[RD2] G. R. van der Werf, J. T. Randerson, L. Giglio *et al.*; Global fire emissions and the contribution of deforestation, savanna, forest, agricultural, and peat fires (1997–2009). *Atmos. Chem. Phys.*; **10** (2010) (23), 11707; doi:10.5194/acp-10-11707-2010.

[RD3] R. Swap, M. Garstang, S. A. Macko *et al.*; The long-range transport of southern African aerosols to the tropical South Atlantic. *J. Geophys. Res.*; **101** (1996), D19; doi:10.1029/95JD01049.

[RD4] M. de Graaf, L. G. Tilstra, P. Wang *et al.*; Retrieval of the aerosol direct radiative effect over clouds from spaceborne spectrometry. *J. Geophys. Res.*; **117** (2012) (D7); doi:10.1029/2011JD017160.

[RD5] Glenn Rolph, Ariel Stein and Barbara Stunder; Real-time Environmental Applications and Display sYstem: READY. *Environ. Modell. Softw.*; **95** (2017), 210 ; doi:10.1016/j.envsoft.2017.06.025.

[RD6] Chamara Rajapakshe, Zhibo Zhang, John E. Yorks *et al.*; Seasonally transported aerosol layers over southeast Atlantic are closer to underlying clouds than previously reported. *Geophysical Research Letters*; **44** (2017) (11), 5818; doi:10.1002/2017GL073559.

[RD7] K. N. Liou; *An Introduction to Atmospheric Radiation* (Academic Press, 2002).

3 References, terms and acronyms

3.1 Terms, definitions and abbreviated terms

AAI	Absorbing Aerosol Index
AAOT	Aerosol Absorption Optical Thickness
AOD	Aerosol Optical (Penetration) Depth
AOT	Aerosol Optical Thickness (partial - layer or total - atmosphere)
ATBD	Algorithm Theoretical Baseline Document
BRDF	Bidirectional Reflectance Distribution Function
BSA	Black-Sky Albedo
CAMS	Copernicus Atmosphere Monitoring Service
CF	Climate and Forecast metadata conventions
DAK	Doubling-Adding KNMI
DU	Dobson Units, 2.69×10^{16} molecules cm^{-2}
ECMWF	European Centre for Medium-Range Weather Forecast
ENVISAT	Environmental Satellite
EOS-Aura	Earth Observing System – Aura satellite
EPS-SG	EUMETSAT Polar System – Second Generation
ERS	European Remote Sensing Satellite
ESA	European Space Agency
EUMETSAT	European Organisation for the Exploitation of Meteorological Satellites
FOV	Field-of-View
FRESCO	Fast Retrieval Scheme for Clouds from the Oxygen A band
GMTED2010	Global Multi-resolution Terrain Elevation Data 2010
GOME	Global Ozone Monitoring Experiment
HDF	Hierarchical Data Format
KNMI	Koninklijk Nederlands Meteorologisch Instituut
LER	Lambertian-Equivalent Reflectivity
LUT	Look-Up Table
L2OP	Level-2 Operational Processor
L2PP	Level-2 Prototype Processor
MERIS	Medium Resolution Imaging Spectrometer
METOP	Meteorological Operational Satellite
MLS	Mid-Latitude Summer
NASA	National Aeronautics and Space Administration
NISE	Near-real-time Ice and Snow Extent
NRT	Near-Real-Time
OMI	Ozone Monitoring Instrument
PAM	Performance Assessment Module
RAA	Relative Azimuth Angle
RMSE	Root-Mean-Square Error
RTM	Radiative Transfer Model
SAA	Solar Azimuth Angle
SCIAMACHY	Scanning Imaging Absorption Spectrometer for Atmospheric Chartography
SW	Software
SZA	Solar Zenith Angle
S5	Sentinel-5 mission

S5P	Sentinel-5 Precursor mission
TOA	Top-of-Atmosphere
TOMS	Total Ozone Mapping Spectrometer
TROPOMI	Tropospheric Monitoring Instrument
UTC	Coordinated Universal Time
UV	Ultraviolet
UVNS	Ultraviolet Visible Near-infrared Shortwave spectrometer
VAA	Viewing Azimuth Angle
VIS	Visible
VZA	Viewing Zenith Angle

4 OMI Instrument description

A description of the OMI instrument and performance can be found in: .

5 MODIS Instrument description

A description of the MODIS instrument and performance can be found in: .

6 Introduction to the Aerosol DRE product

6.1 Background

The aerosol Direct Radiative Effect (DRE) quantifies the energy change due to aerosols interacting with (solar) radiation. The product described here quantifies the amount of energy that is absorbed by smoke that is present above cloud layers, directly interacting with the incoming solar radiation and the radiation reflected by the clouds.

The satellite product DRE is a combination of measurements by the satellite instruments OMI and MODIS, flying within approxamitely 8–15 minutes from each other (see section 4 for details), in an afternoon polar-orbiting constellation. Therefore, the aerosol DRE is measured only once per day for a location on the Earth, and always during the local afternoon (approximately 13.30 local time). Combining measurements from

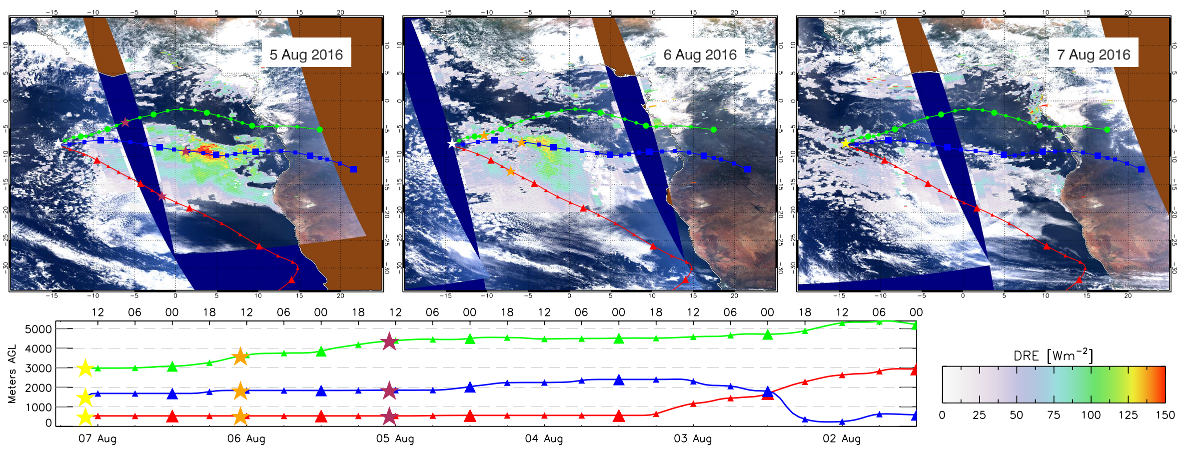

Figure 1: Aerosol DRE over clouds over the south-east Atlantic Ocean during 5–7 August 2016, combined with backtrajectories from the HYSPLIT model, indicating air parcels ending at 500 m (red), 1500 m (blue), and 3000 m (green) at Ascension Island. The position of the air in the backtrajectories during the satellite overpasses is indicated by the coloured stars (yellow on 7 August (at Ascension Island), orange on 6 August, and brown on 5 August).

these two instruments is a computationally very demanding task, and the area for which the aerosol DRE was computed is small, only a large part of the south-east Atlantic Ocean is covered, for all other areas the product is not available. The measurements from the instruments cover the entire shortwave (solar) spectrum (ultraviolet - visible - shortwave infrared), at a high to moderate resolution, so only shorwave absorbed energy is considered. Longwave radiation (emitted by the Earth and atmosphere) is not considered. This means that only small aerosols (i.e. having similar size as the wavelengths of the radiation) are considered here. The most common small sized aerosol found in the area is smoke from biomass burning, and absorption will be assumed to have been due to smoke only. Desert dust, which is also commonly present over the Atlantic, is excluded from the consideration, but dust also absorbs solar energy and introduces uncertainties in the attribution of the product. Smoke absorbs most strongly in the UV, and the absorbed energy is typically highest in the UV. The smoke source over the Atlantic Ocean is typically biomass burning on the African continent during the monsoon dry season [RD1]. Therefore, the aerosol DRE is only computed for the months June–October. During the dry season a myriad of vegetation fires produces immense amounts of smoke, which is the single largest source of black carbon and natural carbonaceous species in the atmosphere worldwide (about 25 Tg black carbon annually [RD2]). The smoke can drift over the Atlantic during westerly circulations. It is most often found in a layer between about 1–5 km altitude, above the marine boundary layer [RD3, RD4].

The aerosol DRE over clouds is therefore defined as the instantaneous energy change due to radiation absorption by smoke above clouds. It is expressed in Wm^{-2}. The derivation is limited to ocean cloud scenes.

High values of the aerosol DRE over clouds are typically found in areas with thick smoke plumes overlying a marine stratocumulus cloud deck in the boundary layer. This is illustrated in Figure 1, where the aerosol DRE is quantified over the Atlantic during three consecutive days (5,6,7 August 2016). It shows the synoptic situation during the satellite overpasses (13:30 local time), using RGB images from MODIS, mainly illustrating the position of the clouds. The clouds in this region are typically extensive fields of marine stratocumulus cloud decks in the boundary layer. The DRE (in Wm^{-2}) is overplotted, showing the places where smoke over the clouds absorbs solar radiation. Overplotted on this are backtrajectories of air parcels ending on 7 August 2016 at 500 m, 1500 m and 3000 m altitude, respectively, over Ascension Island, a small island at 8.0° S, 14.4° W, computed using the HYSPLIT model [RD5]. The position of the air parcel during the satellite overpasses is given exactly by the stars on each day. They show that the plume of smoke that absorbs the large amount of radiation passes over the Atlantic in a few days, in a layer at around 1500–2000 m altitude. Only this layer was over the continent at ground level until 2 August 2016, lifted to about 2000 m, and slowly descending to 1500 m over Ascension Island. The other levels are not clearly connected to the position of the smoke plume.

Another illustration is given below using SCIAMACHY data.

6.2 Heritage

The aerosol DRE was originally developed using SCanning Imaging Absorption spectroMeter for Atmospheric CHartographY (SCIAMACHY) data. SCIAMACHY was a spectrometer on the Environmental Satellite (Envisat) launched in 2002 into a polar orbit with an Equator crossing time of 10:00 LT for the descending node. It had the unique capability to observe a contiguous reflectance spectra from 240 to 1750 nm at a spectral resolution of 0.2 to 1.5 nm. This contains 92% of the energy of the solar spectrum and was used to capture the absorption by UV-absorbing smoke over the Atlantic. SCIAMACHY acquired data alternately in nadir and limb mode, producing data blocks called 'states',approximately 960×480 km^2 in size.

The use of SCIAMACHY data is illustrated in Figure 2. It shows the DRE over the south-east Atlantic ocean on 13 August 2006, when a huge smoke plume is overlying the marine boundary layer stratocumulus cloud deck. The cloud deck is illustrated using an RGB image from MERIS, an imager also on EnviSat. For one SCIAMACHY pixel, where the aerosol DRE is very high, 124 Wm^{-2}, the measured scene reflectance spectrum is shown in red, while the equivalent cloud scene refeflectance spectrum for that scene when no smoke had been present is given blue. The red line represents the spectrum of the aerosol polluted cloud spectrum, while the blue line represents the unpolluted cloud spectrum, which was simulated using a radiative transfer model scheme. The difference between these spectra is due to radiation absorption by aerosols (indicated in yellow). Clearly, the absorption is largest in the UV and disappears in the SWIR. The states are indicated as white rectangles. Over clouds, where no smoke present, the aerosol DRE is low. If no clouds are present, or over land, the aerosol DRE is not computed.

The vertical extend of the smoke and cloud deck can be visualised using lidar data from Calipso on CALIOP. The CALIOP track on 13 August 2006 around 01:25 UTC is shown in Figure 2 as the yellow line. This overpass is very close to SCIAMACHY overpass in space, and about eight hours before the SCIAMACHY measurements. The night time measurements around 01:25 UTC from the Calipso lidar are shown in Figure 3 as a curtain plot, showing the total attenuated backscatter at 532 nm as a function of altitude along the track shown in Figure 2.

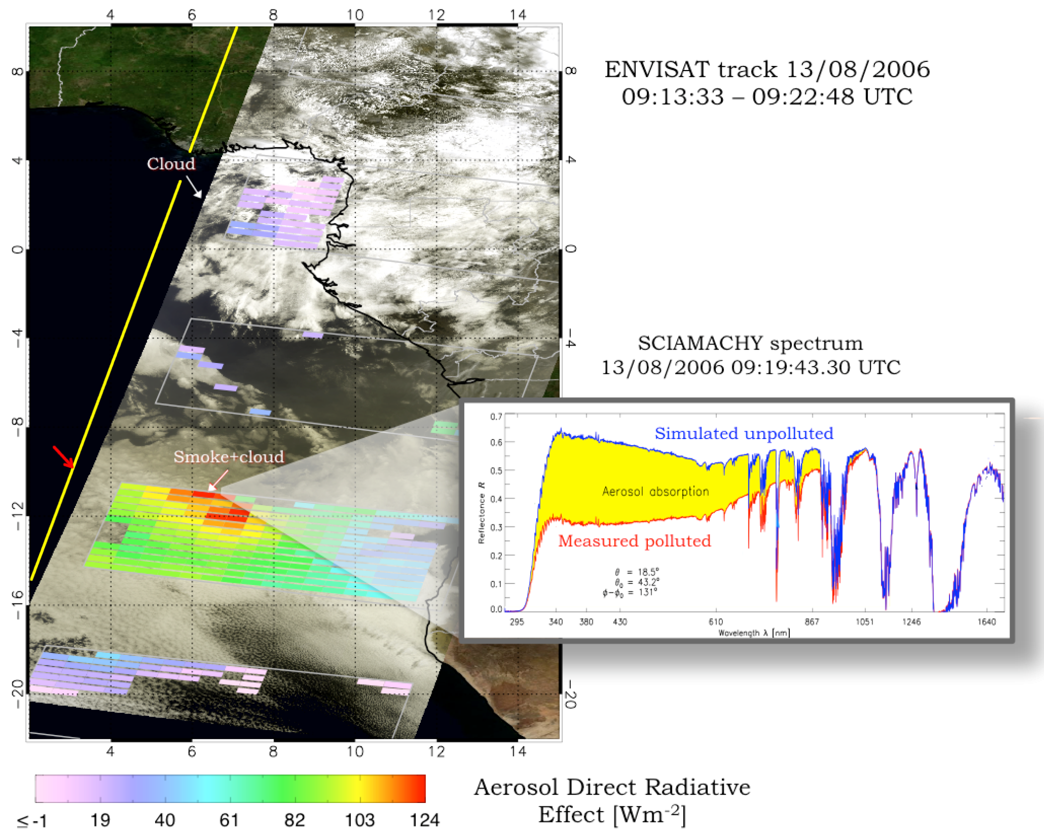

Figure 2: MERIS RGB image on 13 August 2006 around 9:19 UTC, with the SCIAMACHY aerosol DRE over clouds overplotted. The SCIAMACHY spectrum for the pixel with the highest DRE is given in the inset in red, while the equivalent spectrum for the same scene with the same cloud but without the overlying aerosols is given in blue. The CALIOP track around 1:25 UTC is given by the yellow line. The total attenuated backscatter along this track is given in Figure 3. The location of the red arrow corresponds with the location of the red arrow in Figure 3.

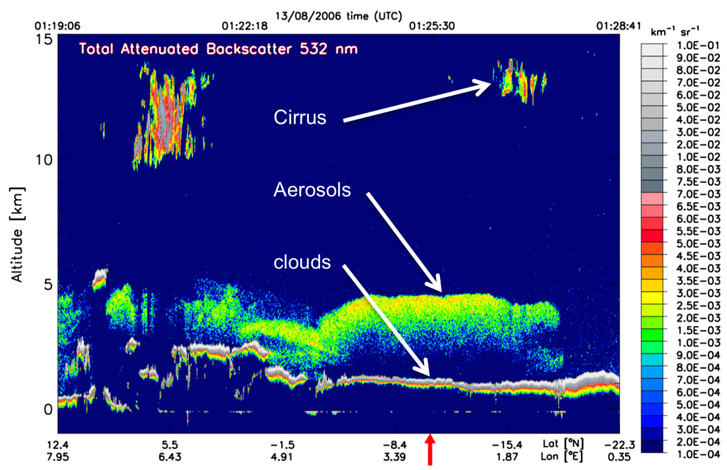

Figure 3: Total attenuated backscatter signal from Calipso in CALIOP, along the yellow track shown in Figure 2. The color scale is such that generally grey colors correspond with clouds, green to red colors correspond with aerosol layers, and blue colors corrspond to clean air. The location of the red arrow corresponds with the location of the red arrow in Figure 2, which is the position of the closest proximity of the CALIOP track to the SCIAMACHY pixel with the highest DRE.

This illustrates the vertical location of the cloud (top) and aerosol plume (top). Note that the lidar beam does not penetrate the cloud, and also saturates in the smoke layer, and the high backscatter signals only indicate the location of the top of the layers, and cannot show the bottom of the layers. Whether the aerosol plume touches the cloud layer or not remains unresolved [RD6]

6.3 Algorithm description

6.3.1 Theory

The radiative effect of an atmospheric constituent can be defined as the net broadband irradiance change $\Delta\mathscr{E}$ at a certain level with and without the forcing constituent, after allowing for stratospheric temperatures to readjust to radiative equilibrium, but with tropospheric and surface temperatures and state held fixed at the unperturbed values. For tropospheric aerosols as the forcing agent, stratospheric adjustments have little effect on the radiative forcing and the instantaneous irradiance change at the TOA can be substituted:

$$\Delta\mathscr{E}_{\text{aer}}^{\text{TOA}} = \mathscr{E}_{\text{with aer}}^{\text{net}} - \mathscr{E}_{\text{without aer}}^{\text{net}}, \tag{1}$$

where $\mathscr{E}^{\text{net}}$ is the net irradiance, defined as the difference between the downwelling and upwelling shortwave irradiances at the TOA, $\mathscr{E}^{\text{net}} = \mathscr{E}^{\downarrow} - \mathscr{E}^{\uparrow}$. Furthermore, the extinction optical thickness of biomass burning aerosols decreases strongly with increasing wavelength. Therefore, biomass burning aerosols do not significantly interact with the longwave (terrestrial) radiation, so the net broadband irradiance can be substituted by the net shortwave irradiance. At the TOA the shortwave downwelling irradiance is the total incoming solar irradiance $\mathscr{E}_0$ for any scene, and $\mathscr{E}^{\downarrow}$ can be eliminated. Consequently, for aerosols overlying a cloud the direct radiative effect is given by

$$\Delta\mathscr{E}_{\text{aer}}^{\text{TOA}} = \mathscr{E}_{\text{cld}}^{\uparrow\,\text{TOA}} - \mathscr{E}_{\text{cld+aer}}^{\uparrow\,\text{TOA}}, \tag{2}$$

where $\mathscr{E}_{\text{cld}}^{\uparrow\,\text{TOA}}$ is the upwelling irradiance at the TOA for an aerosol-unpolluted cloud scene and $\mathscr{E}_{\text{cld+aer}}^{\uparrow\,\text{TOA}}$ is the upwelling shortwave irradiance for an aerosol-polluted cloud scene. By equation (2), if energy is absorbed in the atmosphere by the aerosols, the direct radiative effect is positive.

The aerosol DRE over clouds is determined from shortwave hyperspectral measurements of passive spectro(radio)meters, using measured reflectances of cloud scenes. The primary satellite product here is the Earth reflectance $R(\lambda)$, measured in the shortwave domain as a function of wavelength at a high spectral resolution. The monochromatic reflectance $R(\lambda)$ is defined as the quotient of the upwelling monochromatic radiance $I(\lambda)$ and the downwelling monochromatic solar irradiance $E_0(\lambda)$:

$$R(\lambda) = \frac{\pi I(\lambda)}{\mu_0 E_0(\lambda)}, \tag{3}$$

where μ_0 is the cosine of the solar zenith angle θ_0 and $\mu_0 E_0$ is the solar irradiance incident on a horizontal surface unit at TOA. $R(\lambda)$ is also computed by the RTM at discrete wavelengths. Below, R and all other quantities refer to the TOA.

The monochromatic irradiance $E(\lambda)$ of the reflected radiation can be found by integrating $I(\lambda)$ over the entire hemisphere, weighted by μ, where μ is the cosine of the viewing zenith angle θ. Substituting equation (3) and using polar coordinates (θ,ϕ):

$$E(\lambda) = \frac{\mu_0 E_0(\lambda)}{\pi} \int_0^{2\pi}\int_0^1 R(\lambda;\mu,\phi;\mu_0,\phi_0)\mu\,\mathrm{d}\mu\mathrm{d}\phi, \tag{4}$$

where ϕ_0 and ϕ are the azimuth angles of the solar and viewing directions, respectively. Similarly, the (local) plane albedo A for a scene is defined as the integral of $R(\lambda)$ over the entire hemisphere [RD7]:

$$A(\lambda,\mu_0) = \frac{1}{\pi} \int_0^{2\pi}\int_0^1 R(\lambda;\mu,\phi;\mu_0,\phi_0)\mu\,\mathrm{d}\mu\mathrm{d}\phi. \tag{5}$$

By substituting equation (5) in (4) and integrating over wavelength in the shortwave (SW) domain, equation (2) becomes

$$\Delta\mathscr{E}_{\text{aer}}(\mu_0) = \int_{\text{SW}} \mu_0 E_0(\lambda)\left(A_{\text{cld}}(\lambda,\mu_0) - A_{\text{cld+aer}}(\lambda,\mu_0)\right)\mathrm{d}\lambda. \tag{6}$$

6.3.2 Differential Aerosol Absorption technique

The aerosol DRE over clouds is determined using RTM results for the first term in equation (6), A_{cld}, and measurements of the reflectance $R(\lambda)$ for the second term, $A_{\mathrm{cld+aer}}$. From the RTM results, the plane albedo A_{cld} can be determined from integration of the reflectances in all directions. However, from a satellite instrument only the reflectance in the viewing direction is known. Therefore, the plane albedo for this scene, $A_{\mathrm{cld+aer}}$, must be estimated. A measure for the angular distribution of the reflected radiation for a scene is the anisotropy factor $B(\lambda,\mu_0) = R/A$. The anisotropy factors are assumed to be unchanged by the aerosols over the clouds nad therefore equal for the aerosol-unpolluted and aerosol-polluted cloud scenes, $B_{\mathrm{cld}} = B_{\mathrm{cld+aer}}$.

Then, equation (6) can be rewritten and the instantaneous aerosol direct radiative effect over clouds $\mathrm{DRE_{aer}}$ can be defined as the net shortwave irradiance change at the TOA:

$$\mathrm{DRE_{aer}} = \Delta\mathscr{E}_{\mathrm{aer}}(\mu_0) = \int_{SW} \frac{(R(\lambda)_{\mathrm{cld}} - R(\lambda)_{\mathrm{cld\,+\,aer}})\,\mu_0 E_0(\lambda)}{B(\lambda,\mu_0)_{\mathrm{cld}}}\,\mathrm{d}\lambda + \varepsilon, \tag{7}$$

where $R(\lambda)_{\mathrm{cld}}$ is a simulated aerosol-free cloud reflectance, representative for the measured scene with the aerosols removed. The aerosol DRE follows from the integration of the radiance difference between the simulated aerosol-free cloud scene and measured aerosol polluted cloud scene over the solar spectrum, hence the term differential aerosol absorption was coined. The wavelength integration limits in Eq. 7 were 240 and 1750 nm for the contiguous SCIAMACHY reflectance measurements. In case of combined OMI and MODIS reflectances, the integration limits are from the start of OMI measurements (about 270 nm) to the first of the MODIS channels that are used to invert cloud parameters (1246 nm), where the aerosol absorption is assumed to have become negligible. ε represents all the instrument and retrieval errors of a single measurement, due to the assumptions described above and the measurement uncertainties. These will be quantified in section 8.

An illustration of the DAA technique is given in Fig. 4. The first step is the selection of suitable scenes, i.e. the selection of scenes with clouds; see above. To ensure the selection of (low-level) water clouds, only pixels with a cloud pressure larger than a threshold (e.g. 800 hPa) are selected. Step two is the determination of a measured scene reflectance spectrum. For SCIAMACHY this was trivial; the combination of OMI and MODIS reflectances is treated in Sect.??. Step three is the retrieval of the cloud optical thickness (COT) and cloud droplet effective radius r_{eff}, using the SWIR part of the reflectance determined in step two, (e.g. $R_{1.2\mu\mathrm{m}}$ and $R_{2.1\mu\mathrm{m}}$) and tabulated SWIR reflectances. The fourth step is the simulation of the cloud scene reflectances in the UV, visible and SWIR part of the spectrum. This forward step is also performed using a LUT as before, which contains reflectances at 18 wavelengths from 295 nm to 2130 nm, see section 6.3.6. Once the simulated and measured cloud scene reflectances are available, the DRE is computed in step five, using Eq. 7 and a measured or reference solar irradiance spectrum $E_0(\lambda)$.

6.3.3 Water cloud selection

The pixels are filtered for cloud fractions lower than 0.2 and cloud pressure larger than 800 hPa, using the OMI O2-O2 cloud product.

6.3.4 Measured reflectance extraction

After selection of suitable cloud pixels, a hyperspectral reflectance spectrum is constructed using collocated OMI and MODIS/Aqua pixels. Spectrally, OMI overlaps with MODIS at 459–479 nm (central wavelength 469 nm), which can be used to match the OMI reflectances in the visible channel and the MODIS reflectance in band 3. Spatially, the overlap is more complicated, since the OMI footprint is not uniquely defined due to the use of a polarisation scrambler. The polarisation scrambler projects four depolarized beams onto the detector CCD, which are slightly shifted with respect to each other, and therefore only the central point of the OMI footprint is uniquely defined. Furthermore, since the optics of OMI contain no moving mirror, but projects the incoming radiation onto the CCD detector array directly during a 2 s interval, the spatial response function of the OMI footprints is not box-shaped, but rather Gaussian-shaped in two dimensions. 74 % of the radiance received at a detector pixel is from within the corner coordinates, the rest of the signal is from outside the pixel corner coordinates. The OMI field of view was analyzed in detail in [**?**] and [**?**]. A 2D-Gaussian shape is used here to average MODIS reflectances across the OMI pixel, favoring pixels near the OMI center and allowing for overlapping ground pixels.

The projections of radiation are slightly different in the two OMI UV channels and the OMI visible channel, resulting in slightly different ground pixels and wavelength grids, but these have not been accounted for. All

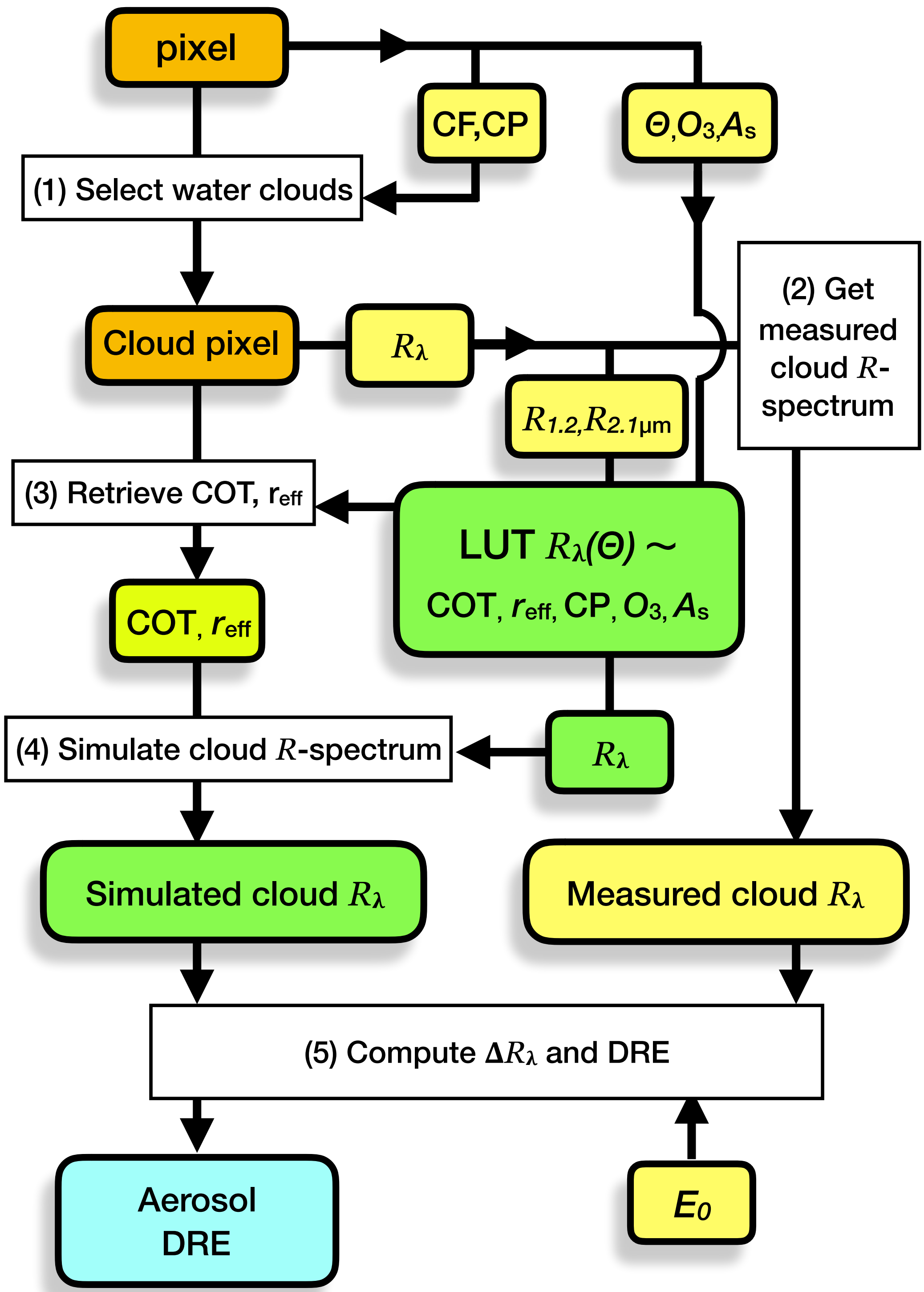

Figure 4: Flow diagram for the Differential Aerosol Absorption technique. Yellow boxes contain pixel products, green boxes contain simulated quantities, the yellow/green box is a retrieval for the cloud pixel and the light blue box is the end product. Θ represents the geometry of the measurements, E_0 is the irradiance spectrum, R_λ is the reflectance (spectrum), CF is cloud fraction, CP is cloud pressure, COT is cloud optical thickness, r_{eff} is cloud droplet effective radius, O_3 is the ozone profile, and A_s is the surface albedo.

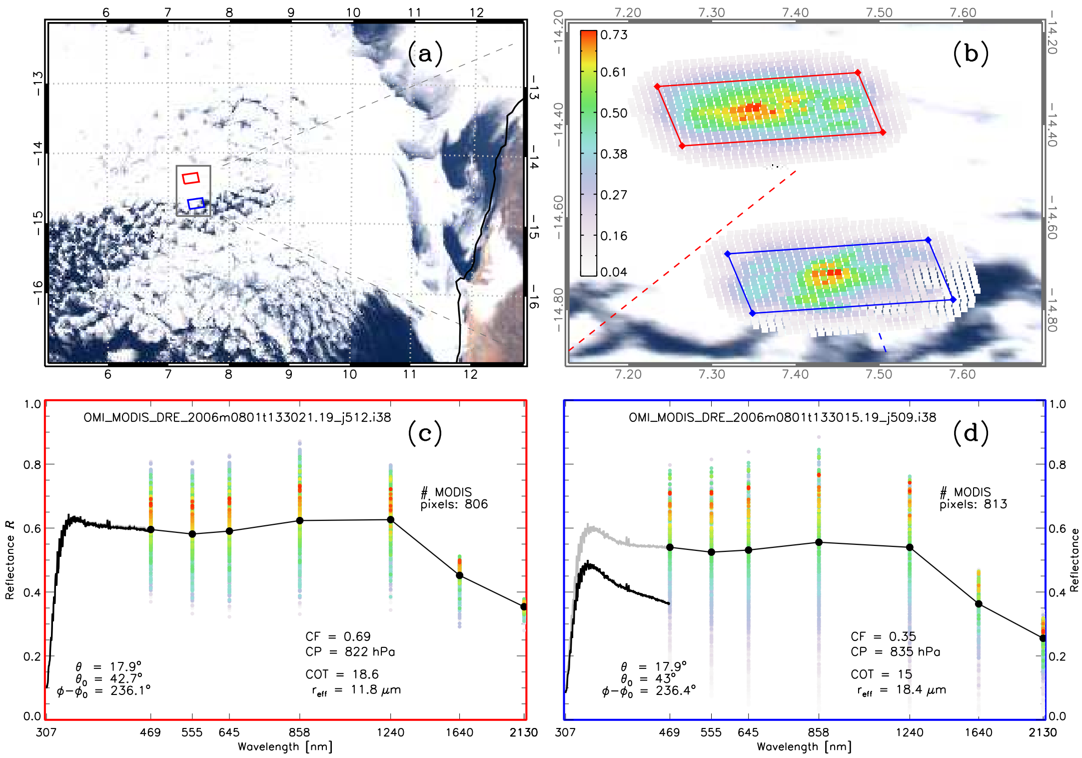

Figure 5: Illustration of the computation of the Aerosol DRE from a combination of one OMI pixel and collocated MODIS pixels. (a) Overview of a stratocumulus cloud deck over the south-east Atlantic Ocean using MODIS RGB and two selected OMI pixels in red and blue on 1 August 2006. (b) Close-up of the two selected OMI pixels, with collocated high-resolution MODIS pixels, coloured by their intensity, which is determined by the MODIS reflectance, convolved with the OMI pixel point spread function that is used to weight the contribution of the individual MODIS pixels. (c) Shortwave spectrum from the red OMI pixel, acquired at 13:30:21 UTC, combined with the average MODIS reflectance (both in black), acquired around 13:14:15 UTC. The coloured dots indicate the weight of the individual MODIS pixels. (d) Shortwave spectrum of the blue OMI pixel, acquired at 13:30:15 UTC (black), and the average of the MODIS pixels, acquired around 13:14:09 (black). The grey curve indicates the OMI spectrum after scaling with the average MODIS spectrum.

computations were performed and reported relative to the wavelength grid and ground pixels of the OMI visible channel.

Two examples of OMI pixels tiled with MODIS pixels are shown in Fig. 5. Figure 5a shows an overview of the situation: a broken cloud field over the south-east Atlantic Ocean, west of Africa, with two OMI pixels, one in the stratocumulus cloud deck (red), and one at the cloud edge (blue). Figure 5b shows the MODIS pixels that are collocated with the OMI pixels, colored by their weight in the averaging of the reflectance, which is the reflectivity convolved with the Gaussian function. Clearly, points close to the OMI pixel center are favored, but also pixels beyond the corner coordinates contribute to the radiation in the pixel. The cloud structure clearly has a large influence on the contributing pixels.

Figure 5c shows the combined OMI-MODIS reflectance of the fully cloudy scene (red), while Fig. 5d shows the combined OMI-MODIS reflectance of the broken cloud scene (blue). Clearly, there is a mismatch between OMI and MODIS for the broken cloud scene, which is caused by changes in the reflectance due to changes in the cloud fraction in the OMI footprint. The average reflectance of the scene has changed during the 15 minutes between overpasses of Aura and Aqua. The OMI/FRESCO effective CF was 0.69 in the red pixel, and 0.35 in the blue pixel. Fifteen minutes earlier, during the MODIS overpass, the geometric MODIS CF was around 0.99 and 0.98, respectively. Note that effective cloud fraction is generally lower than geometric cloud fractions. In order to get a contiguous reflectance spectrum, the average reflectance during the MODIS overpass is taken and OMI was scaled to match the MODIS average reflectance at 469 nm. Scaling MODIS to OMI seemed obvious at first, to have all parameters at the OMI grid and time. However, this resulted in very noisy data, because scaled MODIS reflectances resulted in flawed cloud parameter retrievals at longer wavelengths and the accuracy of the DRE over clouds depends strongly on the accuracy of the cloud parameters. The derivation of cloud parameters is treated below.

6.3.5 Cloud retrieval

In the current implementation, the MODIS reflectances at 1.2 μm and 2.1 μm are used to derive cloud droplet effective radius and cloud optical thickness, following [**?**]. Using wavelengths in the SWIR, instead of the visible, avoids biases of cloud parameters due to absorption by overlying aerosols [**?**]. The cloud parameters retrieved in this way have a larger uncertainty, but can be used for scenes with overlying aerosols [RD4]. Note that the MODIS reflectance at 1.6 μm is not used for the cloud retrieval, because of the large number of bad and dead pixels in the MODIS/Aqua detector [**?**]. The cloud droplet effective radius and cloud optical thickness are used to construct an aerosol-free cloud scene reflectance spectrum using RTM simulations ($R(\lambda)_{\mathrm{cld}}$ in Eq. 7.) Since the retrieval of the DRE is depending so much on the correct cloud parameters and subsequent scene reflectance, the average MODIS reflectances have to be taken as a basis, and OMI reflectances have to be scaled to MODIS. The cloud optical thickness and cloud effective radii are shown in Fig. 5, representing the clouds in the two OMI pixels during MODIS overpass.

6.3.6 Cloud spectrum modelling

The fourth step is the simulation of the cloud scene reflectances in the UV, visible and SWIR part of the spectrum. This step is performed using the cloud pressure and effective cloud droplet radius found before, and extracting the reflectances at 18 spectral points from 295 nm to 2130 nm for these cloud parameters, using the same LUT as before, see Table 1.

Table 1: Spectral cloud reflectance LookUp Table nodes

Parameter	Nodes								
wavelength λ [nm]	295	310	320	330	340	380	430	469	555
	610	645	858	867	1051	1240	1246	1640	2130
cloud optical thickness τ_{cld}	2	4	8	12	16	20	24	32	48
droplet size r_{eff} [μm]	3	4	6	8	12	16	20	24	
cloud base height z_{cld} [km]	0	1	4	8	12				
total O_3 column Ω [DU]	267	334	401						
surface albedo A_s	0	0.5	1						
droplet size eff. variance v_{eff}	0.15								
number of θ_0, θ, $\phi-\phi_0$	14	14	19						

6.3.7 Direct radiative effect computation

The final step is the derivation of the direct radiative effect using the spectral difference between the simulated and measured spectrum. The reflectance differences at the 18 wavelength nodes are interpolated and multiplied using a high resolution irradiance spectrum, to find the radiance difference This is then divided by the anisotropy factor for the cloud scene and interpolated from the UV to SWIR, see Eq. 7. The last step is illustrated in Fig. 6.

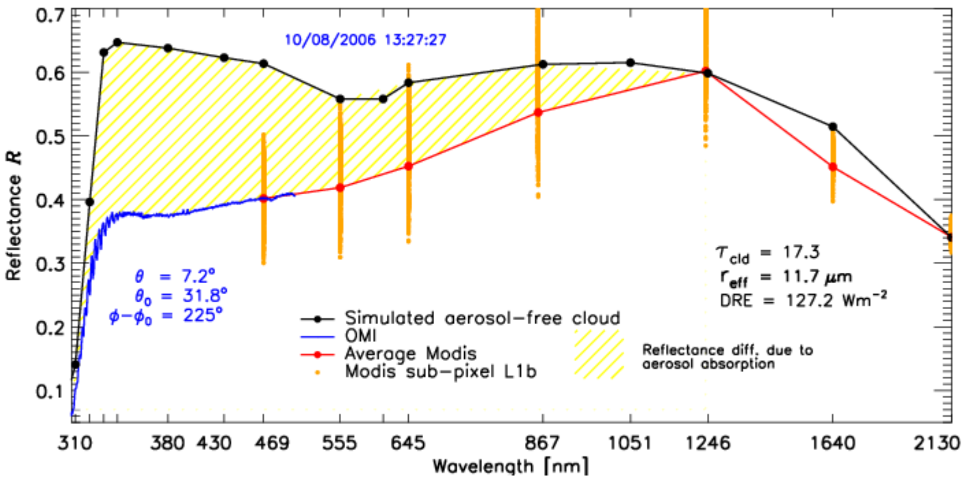

Figure 6: The differential Aerosol Absorption technique illustrated with a combined OMI and MODIS spectrum. In blue the spectrum measured by OMI is given for the pixel indicated by the blue arrow in Fig. 7, and in red the MODIS average spectrum for this pixel. The black solid line shows the simulated aerosol-free cloud spectrum computed with an RTM for the OMI pixel. The yellow shaded part shows the reflectance difference for this pixel. The orange dots show the range of reflectance values at the different MODIS channels in this OMI pixel, the red dot is the weighted average reflectance.

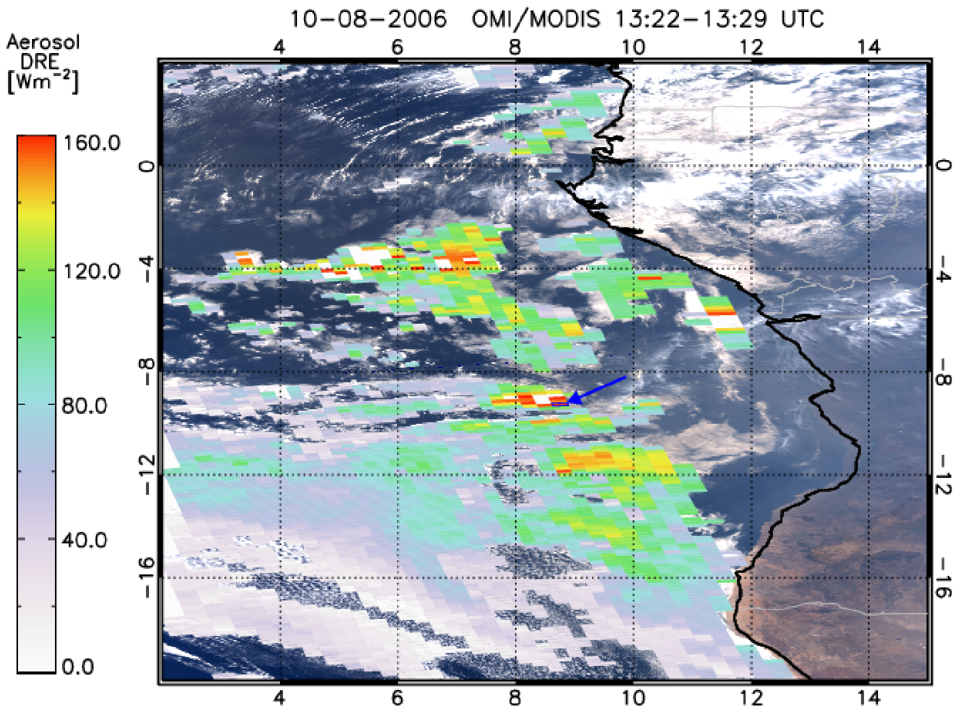

Figure 7: Instantaneous aerosol direct radiative effect (DRE) over clouds on 10 August 2006 from a combination of OMI and MODIS reflectances, overlaid on a MODIS RGB image. The reflectance spectrum of the pixel indicated by the blue arrow is given in Fig. 6.

7 Feasibility

TBW

8 Error Analysis

TBW

9 Validation

TBW

10 Conclusion

This ATBD is in preparation phase.